# We are IntechOpen,
# the world's leading publisher of
# Open Access books
# Built by scientists, for scientists

## 6,900
Open access books available

## 185,000
International authors and editors

## 200M
Downloads

## 154
Countries delivered to

Our authors are among the

## TOP 1%
most cited scientists

## 12.2%
Contributors from top 500 universities

**CLARIVATE ANALYTICS**
**BOOK CITATION INDEX**
**INDEXED**

**WEB OF SCIENCE™**

Selection of our books indexed in the Book Citation Index
in Web of Science™ Core Collection (BKCI)

# Interested in publishing with us?
# Contact book.department@intechopen.com

Numbers displayed above are based on latest data collected.
For more information visit www.intechopen.com

# Near- and Middle-Infrared Monitoring of Burned Areas from Space

*Carlos C. DaCamara, Renata Libonati, Miguel M. Pinto and Alexandra Hurduc*

## Abstract

We describe a methodology to discriminate burned areas and date burning events that use a burn-sensitive (V, W) index system defined in near-/mid-infrared space. Discrimination of burned areas relies on a monthly composite of minimum of W and on the difference between this composite and that of the previous month. The rationale is to identify pixels with high confidence of having burned and aggregate new burned pixels on a contextual basis. Dating of burning events is based on the analysis of time series of *W,* and searching for the day before maximum temporal separability is achieved. The procedure is applied to the fire of Monchique, a large event that took place in the southwest of Portugal in August 2018. When the obtained pattern of burned pixels is compared against a reference map, the overall accuracy is larger than 99%; the commission and omission errors are lower than 5 and 10%, respectively; and the bias and the Dice coefficient are above 0.95 and 0.9, respectively. Differences between estimated dates of burning and reference dates derived from remote-sensed observations of active fires show a bias of 0.03 day and a root mean square difference of 0.24 day.

**Keywords:** burned area, dates of burning, (V, W) index system, VIIRS sensor, Monchique fire (Portugal)

## 1. Introduction

Vegetation fires have significant direct and indirect impacts on all components of the Earth system, including the anthroposphere. They are a source of greenhouse gases, aerosols, and trace gases to the atmosphere [1–3]; they induce modifications in most radiative forcing terms [4, 5] and disturb the radiative budget and cloud microphysics [6, 7]; they lead to changes in soil properties [8] and in the hydrological cycle [9–11]; they play a key role in biodiversity reduction, loss of genetic diversity, forest ecosystem functioning [12, 13], and land use/cover dynamics [14–16]; and they cause damages to human health [17, 18] and have adverse effects on public health and economy [19].

A thorough understanding of spatial and temporal patterns of burned area (BA) by wildfires is therefore of fundamental importance when assessing either climate or anthropogenic influences on the Earth system [20, 21]; when addressing a very wide range of subjects that include the fields of atmospheric physics and chemistry,

ecology, agriculture and forestry, hydrology, biology, sociology, and economy; and when defining climate, environment, and health policies [22–26]. When specifically focusing on fire management that comprises fire prevention, fire presuppression, and fire suppression measures, reliable information about the extent, location, and time of occurrence of BA is of high added value [25]. Accurate BA information is also crucial to land and fire decision-makers, as well as to research groups and ecologists, government agencies, and NGOs when implementing environmental policies aiming to reduce socioeconomic impacts from vegetation fires on ecosystems and people [27].

The use of remotely sensed information for BA detection is well established, and there is a consensus about its usefulness from global down to regional levels [28–32]. Spaceborne sensors are a cost-effective way to map vegetation fires and the unique source of information for large areas with limited access at regional and global scales and for continuous monitoring over time [33, 34]. Over the last decades, several initiatives have been carried out to generate global and regional long-term maps of BA using remote sensing. These include, among others, (1) the 1-km L3JRC product, covering the period from April 2000 to March 2007, produced from SPOT VEGETATION data [35]; (2) the 1-km GLOBCARBON BA product, spanning the period April 1998–December 2007, derived from SPOT VEGETATION, Along Track Scanning Radiometer (ATSR-2), and Advanced ATSR (AATSR) imagery using a combination of mapping algorithms [36]; (3) the MCD45 [37] and MCD64A1 [30] BA products derived by NASA using data collected by the Moderate Resolution Imaging Spectroradiometer (MODIS); (4) the Global Fire Emissions Database (GEFD) initiative that consists in monthly BA estimates aggregated at 0.5° spatial resolution, covering the period from July 1996 to mid-2009 using four satellite data sets [38]; (5) the AQM-MODIS product [39] that was derived for Brazil and consists in monthly maps of BA at 1 km spatial resolution from 2000 up to the present; (6) the global burned area algorithm based on Medium Resolution Imaging Spectrometer (MERIS) reflectance and MODIS hotspots from 2006 to 2008 [29]; and (7) the recent global burned area product based on MODIS bands with a spatial resolution of 250 m [40].

Remote-sensed detection of burned vegetation makes use of spectral bands that are sensitive to spectral changes induced by fire events [41], namely, those associated to the deposit of char and ash on the surface and the change or destruction of vegetation structure [33]. Spectral indices have revealed to be the most appropriate to uncover changes in the radiometric signals of surfaces in operational applications [42], and a large variety of spectral indices for burned area discrimination have been developed in the last decades using a variety of techniques and different spectral bands, such as the red (R, about 0.6–0.7 μm), the near infrared (NIR, about 0.7–1.3 μm), the shorter short-wave infrared (SSWIR, about 1.3–1.9 μm), and the longer short-wave infrared (LSWIR, about 1.9–2.5 μm). Developed approaches include, among others, the Burned Area Index (BAI) [43] based on R and NIR and its improved version BAIM [44] based on NIR and LSWIR, the NIR and LSWIR-based Normalized Burn Index (NBI) [45], the Normalized Burn Ratio (NBR) [46] and derived indices from the latter [47–51], and the Mid-Infrared Burned Index (MIRBI) [52] based on SSWIR and LSWIR.

A burn-sensitive vegetation index system, the so-called (V, W) system, has also been defined on the NIR/MIR space with the aim of optimally discriminating burned vegetation [53, 54]. Here we present and discuss the use of the (V, W) index system to design an automated algorithm aiming at both mapping burned area and dating the associated burning events. As an example of application, the procedure is applied to the fire of Monchique, a large event that took place in the southwest of Portugal in August 2018 (**Figure 1**).
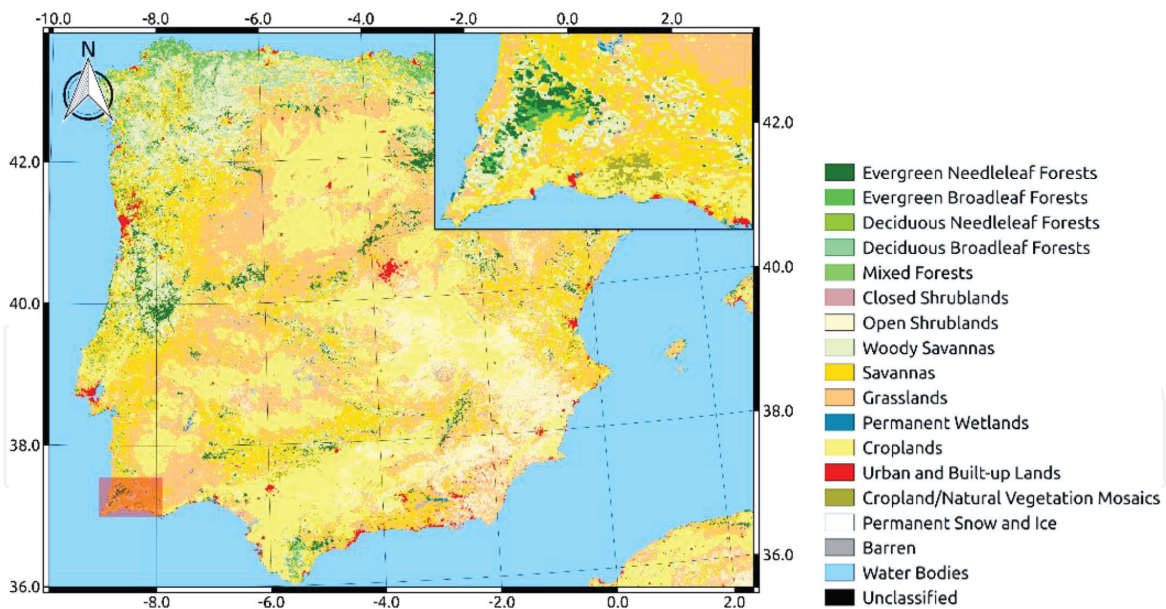
**Figure 1.**
*Land cover map of the Iberian Peninsula showing the geographical location (shaded rectangular area) and a zoom (top right box) of the study area near the southern coast of Portugal (source of land cover data: Modis collection 6 global land cover, https://lpdaac.usgs.gov/sites/default/files/public/product_documentation/mcd12_user_guide_v6.pdf ).*

The fire of Monchique started on August 3 about noon and was not dominated until August 9. The fire resulted in about 27,000 hectares of burned area, 41 people injured and millions of euros in economic losses. By the second day of the event, about 700 firefighters and 11 aerial resources were fighting the fire, and this number kept increasing up to about 1400 firefighters and 14 aerial resources. The fire occurred within a context of very high temperatures and intense and highly variable winds in terrain with difficult access and high accumulation of biomass.

## 2. Data and pre-processing

Input data to the algorithms to compute (V, W) consist of top-of-the-atmosphere (TOA) values of middle-infrared (MIR) and thermal-infrared (TIR) radiances and of near-infrared (NIR) reflectance, as acquired by the Visible Infrared Imaging Radiometer Suite (VIIRS) instrument on board of the joint NASA/NOAA Suomi National Polar-Orbiting Partnership (Suomi-NPP) satellite [55]. VIIRS data were reprojected onto a geographical grid of 0.0045° in latitude by 0.0059° in longitude, corresponding to about 500 m in spatial resolution. Data over Portugal, covering the period of July and August 2018, were extracted from the VIIRS/NPP Level 1B 375 m product [56] and correspond to bands I2 (NIR, centered at 0.865 μm), I4 (MIR, centered at 3.74 μm), and I5 (TIR, centered at 11.45 μm).

Geolocation data, as well as land/sea mask and solar and view angle information for each VIIRS tile, were obtained from the VIIRS geolocation product (VIIRS/NPP Imagery Resolution Terrain-Corrected Geolocation). Values of MIR reflectance were then computed using VIIRS bands I4 (MIR) and I5 (TIR) radiances [57]. All images acquired at solar zenith angles (SZA) greater than 55° were rejected, and, when more than one image was available for the same day, the image selected was the one with the lowest solar zenith angle (SZA). Images used as input to the algorithm for burned area discrimination were further restricted to those with view zenith angles (VZA) not exceeding 45° in order to prevent large distortions in pixel size [53].

Information about active fire data was obtained from the VIIRS 375 m Active Fire product [58]. Finally, radiative power data were obtained from the fire radiative power (FRP) product developed by the Land Surface Analysis Satellite Application Facility (LSA SAF); this product is derived from data acquired by the Spinning Enhanced Visible and Infrared Imager (SEVIRI) onboard Meteosat Second Generation (MSG) series of EUMETSAT geostationary satellites [59].

A reference map of burned area in the study region was derived from geo-spatial information provided by the Rapid Mapping products of the Copernicus Emergency Management Service (EMS) [60]. The Copernicus EMS service was activated by the Portugal National Authority for Civil Protection on August 5 at 16:11 UTC (reference code EMSR303). We used the Delineation Map provided as of August 10 that has an estimated geometric accuracy of 5 m or better, derived by visual interpretation from Sentinel-2 and SPOT satellite observations.

## 3. Methods

### 3.1 Simplified (V, W)

Specially designed to discriminate burned areas, the (V, W) burn-sensitive vegetation index system is defined in a transformed MIR/NIR space that allows enhancing the spectral information about burned vegetation [53]. The transformed space is framed by the following two coordinates: (1) the distance, $\eta$, of each point in MIR/NIR space to a predefined convergence point, representative of a given target (e.g., a totally burned surface) and (2) the difference, $\xi$, between the respective MIR and NIR reflectance of each point. The coordinates $\eta$ and $\xi$ are accordingly defined as

$$\eta = \sqrt{\left(\rho_{MIR} - \rho^0{}_{MIR}\right)^2 + \left(\rho_{NIR} - \rho^0{}_{NIR}\right)^2} \qquad (1)$$

$$\xi = \rho_{MIR} - \rho_{NIR} \qquad (2)$$

where $\rho_{MIR}$ and $\rho_{NIR}$ represent values of reflectance in MIR and NIR and $\left(\rho^0_{MIR}, \rho^0_{NIR}\right)$ are the coordinates of an ideally totally burned pixel.

Values of $\rho^0_{MIR}$ and $\rho^0_{NIR}$ for a given sensor may be estimated by the upper (lower) bound of reflectivity in MIR (NIR) for a large sample of recently burned pixels. To estimate these values for the VIIRS sensor, we used a sample of burned regions for several fires in central Portugal that occurred in 2017. Obtained estimates are $\rho^0_{MIR} = 0.29$ and $\rho^0_{NIR} = 0.06$.

The coordinate system (V, W) is then defined in the MIR/NIR space such that the following properties are met: (1) the V coordinate has a very small dispersion for pixels associated to surfaces containing organic matter and (2) the W coordinate increases with increasing water content of vegetated surfaces. Burned vegetation is characterized by very low values of *W* and by a sharp decrease of *W* following a fire event [53], both characteristics being especially conspicuous in monthly minimum composites of W and of differences of W between a given month and the previous one (**Figure 2**). In turn, non-vegetated surfaces like clouds and water bodies are characterized by low values of V.

Unlike VI3 [57] and GEMI3 [33], the (V, W) index system has the advantage of not having been heuristically derived; however, unlike traditional indices that rely on simple algebraic expressions and are easy to implement by users, the
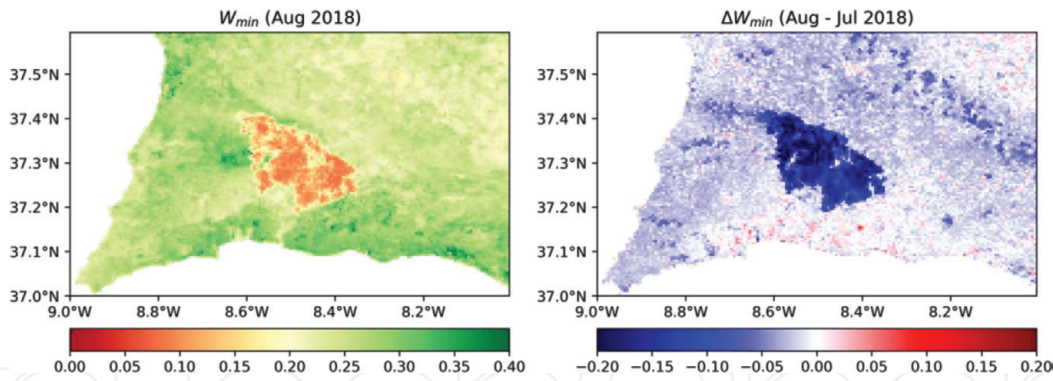
**Figure 2.**
*Spatial distribution over the study area of the minimum composite of $W_{min}$ for August 2018 (left panel) and of the difference of minimum composites of $W_{min}$ between August and July 2018 (right panel).*

computation of (V, W) is laborious, involving iterative methods and numerical computation of line integrals [53]. This disadvantage is circumvented by using the following approximation that is valid in a subdomain of the MIR/NIR space where the majority of observed values are located [54]:

$$V = \frac{(0.16 - 0.71\xi)}{\eta} \quad (3)$$

$$W = 1.1\eta \quad (4)$$

## 3.2 Discrimination of burned areas

Discrimination of burned areas for a given month is based on a procedure that uses as inputs a monthly composite of minimum of W and the difference between this minimum composite and that of the previous month together with locations of all identified hotspots during the considered month [39].

The rationale is first to identify burned pixels with high confidence of being burned and then use these points as seeds in a growing algorithm that will identify other burned pixels on a contextual basis and aggregate them as new seed points. Several studies [39, 61] have pointed out that the vast majority of hotspots are located inside or in the neighborhood of a burned area and that the number of burned pixels that are not close to a hotspot is low.

As suggested by results shown in **Figure 2**, the first seed points are therefore pixels characterized by (1) a low value of the monthly minimum composite of index W and (2) a sharp decrease in that minimum compared to the previous month.

Burned pixels are also expected to be outliers in respect to the statistical distribution pixels where no hotspots were identified. Commonly used in classification problems, the Mahalanobis distance is a measure of the distance of a point to a given distribution in units of the standard deviation in the direction to the point to the mean [62]. The square of the Mahalanobis distance in a p-dimensional space has a chi-square distribution with p degrees of freedom, a result that may be used to find outliers in a dataset [63].

Identification of burned pixels is accordingly performed in the following three steps:

- First step: Let *W min* and *Δ W min* be the values for a given pixel of the monthly composite of minimum W and of the difference between this

5

composite and that of the previous month; the pixel is considered as burned if all three following conditions are met:

- $W_{min} \leq T1$, where $T1$ is a predefined threshold.

- $\Delta W_{min} \leq T2$, where $T2$ is a predefined threshold.

- The pixel lies outside the ellipse defined in the two-dimensional space $(W_{min}, \Delta W_{min})$ that corresponds to a predefined percentile of the Mahalanobis distance computed using pixels where no hotspots were identified; given that only pixels in the quadrant with lower $Wmin$ and $\Delta Wmin$ should be considered as burned, a given pixel is considered as burned if the Mahalanobis distance is above the predefined percentile (e.g., percentile 95) and values of $Wmin$ and $\Delta Wmin$ are sufficiently low, that is, below another predefined percentile (e.g., percentile 10, for both quantities).

- Second step: Let each pixel classified as burned in the previous step be considered as a seed point. For each seed point, a $5 \times 5$ buffer matrix is defined centered on it, and let $N$ be the number of seed points inside it. If $N \geq 3$, let $\hat{W}_{min}$ and $\delta W_{min}$ be the mean and the mean absolute deviation of W for these pixels. Let $W^*_{min}$ and $\Delta W^*_{min}$ be the values of $W_{min}$ and $\Delta W_{min}$ for a pixel inside the $5 \times 5$ buffer matrix that is not a seed point. This pixel is classified as burned and becomes a new seed point if all two following conditions are met:

- $\Delta Wmin* < 0$

- $\Delta Wmin* \leq \hat{W}_{min} + \delta W_{min}$

- Third step: The previous step is repeated until no more seed points are generated.

## 3.3 Dating burned events

For each burned pixel identified by the algorithm above-described, the date of burning is estimated by analyzing the time series of W for that pixel and searching for the day where maximum temporal separability is achieved [64]. For most cases, time series of W present daily fluctuations of rather small amplitude (**Figure 3**) which allows identifying the day when the burning event took place by the significant decrease in W following the event. The day of burning may accordingly be identified as the one that maximizes the following index of temporal separability [65]:

$$S = \frac{2(\mu_b - \mu_a)}{\sigma_a + \sigma_b} \tag{5}$$

where $\mu_a(\sigma_a)$ are the values of the mean (standard deviation) of index $W$ of that pixel for a pre-specified number k of images starting at a given instant in time and $\mu_b(\sigma_b)$ are the respective values for the same k number of images before that instant in time. The time series of W is scanned by two juxtaposed windows of fixed length $k$, and index $S$ is computed for every available day (**Figure 3**). The burning event is considered to have taken place in the day prior to the date when $S$ is maximized.

## 3.4 Validation procedures

### 3.4.1 Discrimination of burned areas

The Monchique BA was validated against the data obtained from the Copernicus Emergency Management Service (EMSR303) that is used as the reference map. The
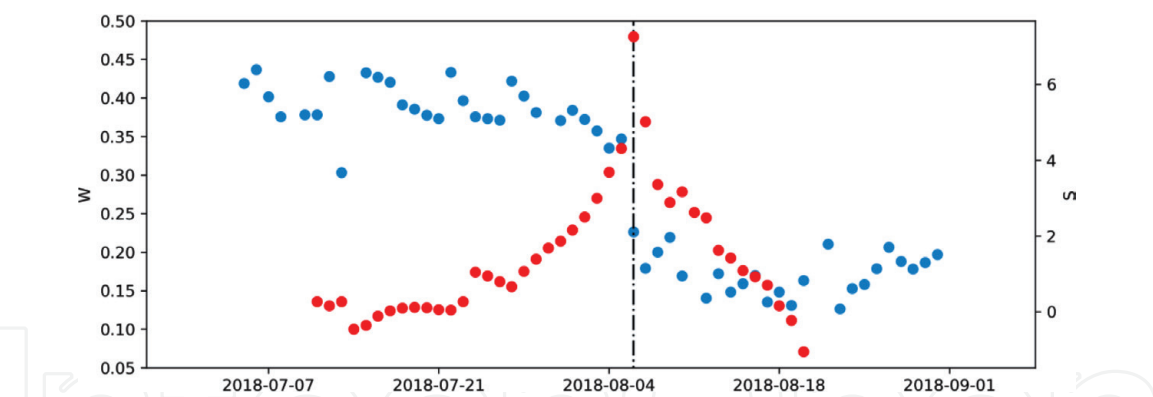
**Figure 3.**
*Time series of indices W (blue dots, left vertical scale) and S (red dots, right vertical scale) for a pixel located inside the burned scar. The vertical black dashed line indicates the day of maximum S (Eq. (5)).*

| Classification map | Reference map | | |
|---|---|---|---|
| | **Burned** | **Unburned** | |
| Burned | a | b | a + b |
| Unburned | c | d | c + d |
| | a + c | b + d | a + b + c + d |

**Table 1.**
*Contingency table for pixels classified as burned versus unburned.*

| OA | OE | CE | B | DC |
|---|---|---|---|---|
| $\dfrac{a+d}{a+b+c+d}$ | $\dfrac{c}{a+c}$ | $\dfrac{b}{a+d}$ | $\dfrac{a+b}{a+c}$ | $\dfrac{2a}{2a+b+c}$ |

**Table 2.**
*Accuracy (OA), omission error (OE), commission error (CE), bias (B), and dice coefficient (DC), with a, b, c, and d as defined in* **Table 1**.

quality of the classification map was assessed based on five verification measures derived from contingency tables [39]: overall accuracy (OA), omission error (OE), commission error (CE), bias (B), and Dice coefficient (DC). These verification measures are defined in **Table 2**. The agreement between the BA scar and the reference map is measured by the OA, a high value of OA reflecting a high accuracy in the classification. OE and CE are used to assess the discriminative power of the classifier. The bias should be close to one when burning events are not overestimated/underestimated. Finally, DC measures the similarity between the reference and the classification maps by overlapping the classified burned pixels to the "truly burned" pixels in the reference map.

Since the reference map has a higher resolution than the classification map, the former was projected onto the 500 m resolution grid of the latter by computing the burned fraction inside each coarser pixel. The pixel was then considered as burned if the fraction of burned area was greater than 0.5.

### 3.4.2 Dating burned events

Validation of estimated dates of burning was made against data of radiative power from the FRP product developed by the LSA SAF [59]. This product, together with three other active fire products derived from SEVIRI imagery, was compared

against active fire data collected by the MODIS sensor, and results obtained showed a higher detection rate of active fire pixels than the other products [66]. Albeit presenting a coarser resolution of about 4 km in the study region, the repeat cycle of 15 min by the SEVIRI instrument allows for a much better temporal resolution than when comparing against VIIRS or MODIS active fires that have only two samples per day. Furthermore, the VIIRS active fires at 375 m resolution were already used in the algorithm to discriminate burned areas and therefore should not be used for validation purposes. The estimated date of each pixel classified as burned was compared to the date of observation of the nearest SEVIRI pixel where a hotspot was identified. Obtained differences between the dates of the burning of the classified burned pixels and the dates of hotspots identified by the SEVIRI instrument were then used to assess the performance of the dating methodology.

## 4. Example of application

The above-described procedure was applied to the study region in the southwest of Portugal in order to discriminate burned pixels during the Monchique fire episode and then estimate the respective date of burning.

As described in Sections 3.1 and 3.2, the identification of burned areas in the study region relies on monthly minimum composites of W for August (**Figure 2**, left panel) and of differences between the minimum composite of August and that of July (**Figure 2**, right panel), hereby referred to as $W_{min}$ and $\Delta W_{min}$, respectively. Both composites were obtained from daily values of $w$ as derived from reflectance values of MIR and NIR from all available VIIRS images with SZA not exceeding 55° and VZA not exceeding 45°.

When values of $W_{min}$ and $\Delta W_{min}$ for all pixels over the study region are represented in a scatter plot (**Figure 4**), two clusters may be identified: (1) one that is formed by a dense cloud with a large number of points that mostly spread over the subarea of the plot that is lower bounded by percentile 10 of the distribution of $W_{min}$ (identified in the plot by the orange-dashed horizontal line) and left bounded by percentile 10 of the distribution of $\Delta W_{min}$ (identified by the orange-dashed vertical line) and (2) a second cluster that is composed of a less dense cloud with a lower number of points that occupy the subarea that is upper bounded by percentile 10 of the distribution of $W_{min}$ and right bounded by percentile 10 of the distribution of $\Delta W_{min}$.

The second cluster, formed by points with low values of both $W_{min}$ and $\Delta W_{min}$, is therefore likely to be associated to burned pixels. Moreover, also as to be expected in case of burned surfaces, the second cluster contains a very large fraction of pixels where hotspots were identified from the VIIRS Active Fire product (plotted as red dots). However, there are points (plotted as green dots) in the second cluster that are not associated to any hotspot, and there are also points in the first cluster that are associated to a hotspot, despite the fact that the large values of both $W_{min}$ and $\Delta W_{min}$ are not consistent with the characteristic signature of a burned pixel. Both situations are to be expected, since (1) a pixel may burn with no active fire having been spotted by VIIRS (e.g., because of cloud or smoke screening, or because the burning took place between passages of the satellite) and (2) an identified active fire may have originated a burned area that represents a small fraction of the area of the pixel, and therefore the radiometric signature is not strong enough to be detected. Both difficulties may be circumvented in part by selecting a set of pixels with high confidence of being burned as seed points to feed into a growing algorithm.

As discussed in Section 3.2 (first step of the algorithm), seed points are defined as pixels belonging to a region of the space ($W_{min}, \Delta W_{min}$) where there is a high
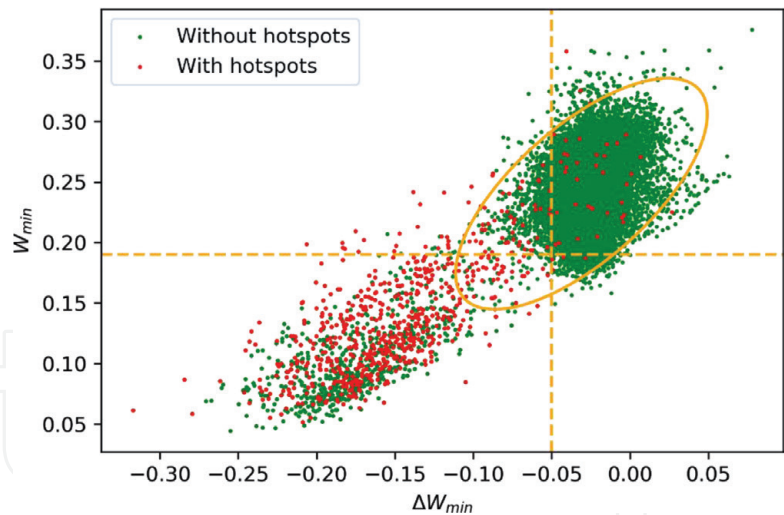
**Figure 4.**
*$W_{min}$ (August 2018) versus $\Delta W_{min}$ (difference between August and July 2018). Red (green) dots indicate pixels with (without) hotspots associated. The orange ellipse represents percentile 95 of the Mahalanobis distance, and the horizontal (vertical) orange-dashed line represents percentile 10 of the distribution of $W_{min}$ ($\Delta W_{min}$).*

confidence that points are associated to burned pixels. Taking into account the above-discussed features presented by the distribution of points in the scatter plot (**Figure 4**), seed points were defined according to the following criteria:

- $W_{min}$ < percentile 10 of $W_{min}$.

- $\Delta W_{min}$ < percentile 10 of $\Delta W_{min}$.

- Points ($Wmin, \Delta Wmin$) must lie outside the ellipse representing percentile 95 of the Mahalanobis distance computed with all pixels not associated to any hotspot.

Once seed points were identified, new burned pixels were then iteratively aggregated following the procedure described in Section 3.2 (second and third steps of the algorithm).

Results obtained are shown in **Figure 5** that also provides a comparison with the reference map that was obtained from information derived from the Copernicus EMS (EMSR303). There is an overall agreement between the down-scaled higher-resolution reference map and the map generated by the proposed algorithm. Deviations from the reference map, either in the form of commission or omission errors, are located along the borders of the scar and are likely to be due to small errors in geolocation or of partially burned pixels that were differently classified (as burned or unburned) by the proposed algorithm and the downscaled reference map.

The overall quality of the proposed algorithm in discriminating the burned pixels associated to the Monchique fire episode reflects on values of the contingency table that compares results from the proposed algorithm with those from the reference map from Copernicus EMS (**Table 3**) as well as on the five verification measures derived from the obtained contingency table (**Table 4**). The number of commission errors (45) and the number of omission errors (94) are one order of magnitude lower than the number of match ups (979). In turn, the overall accuracy is larger than 99%, the commission error is lower than 5%, and the omission error is lower than 10%; the bias is above 0.95, and the Dice coefficient is above 0.9.
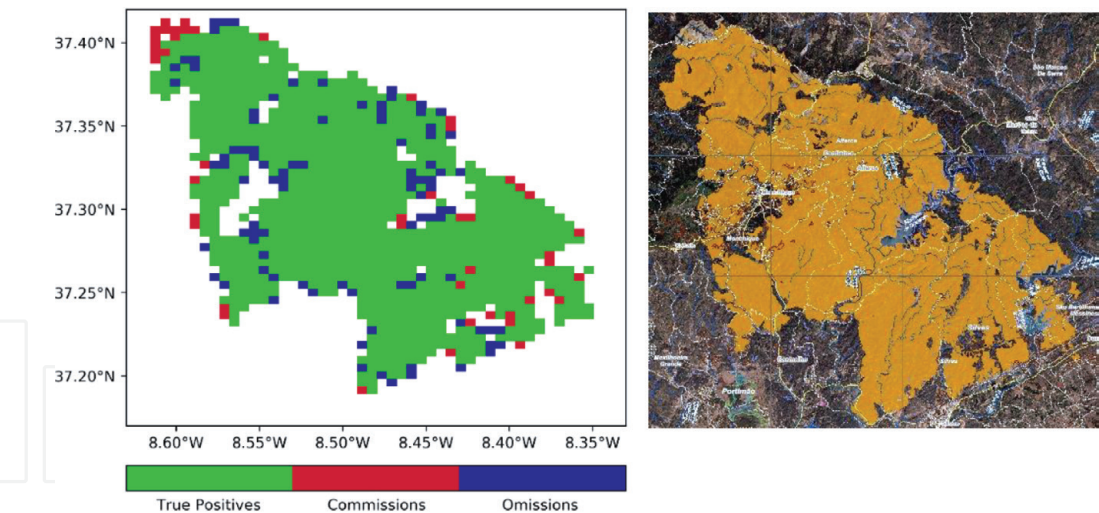
**Figure 5.**
*Burned pixels (left panel) from the proposed algorithm and reference map (right panel) from Copernicus EMS (EMSR303). True positives, commission errors, and omission errors are colored in green, red, and blue, respectively.*

| BA scar | Reference map | | |
|---|---|---|---|
| | **Burned** | **Unburned** | |
| Burned | 979 | 45 | 1026 |
| Unburned | 94 | 21,357 | 21,451 |
| | 1073 | 21,404 | 22,477 |

**Table 3.**
*As in **Table 1** but with values obtained for the scar that resulted from the Monchique fire event of August 2018.*

| OA | OE | CE | B | DC |
|---|---|---|---|---|
| 99.4% | 8.8% | 4.6% | 0.96 | 0.93 |

**Table 4.**
*As in **Table 2** but with the metrics derived from **Table 3**.*

Following the procedure described in Section 3.3, estimates were obtained of the date of burning for all pixels that were classified as burned within the study region. Results obtained (**Figure 6**, left panel) show a propagation from NW to SE, forming a pattern that is very similar to the one derived from the dates of detection of hotspots by the SEVIRI instrument (**Figure 6**, right panel). The agreement between the latter dates and the estimates by the proposed dating algorithm reflects on the obtained histogram of differences that has the null value of differences as the modal frequency, closely followed by a delay of 1 day in the estimates, such that about 70% of the pixels classified as burned have differences in the dates of less than ±1 day. When considering the distribution of differences as a whole, there is a bias of −0.03 day and a root mean square difference of 0.24 day, both values pointing out the very good overall agreement between estimates from the proposed algorithm and the reference dates derived from SEVIRI (**Figure 7**).

Results obtained using a similar procedure over the whole territory of Portugal for August and September 2005, one of the worst severe years in terms of burned area, [64] present an overall accuracy of 95.6% and commission and omission errors of 66.5 and 37.1%, respectively. However, the study encompasses a period of
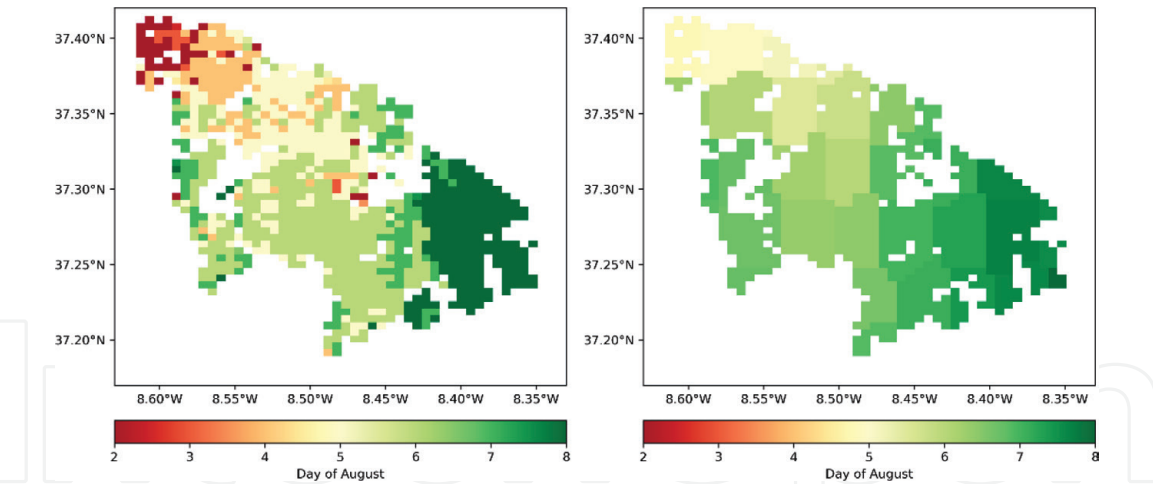
**Figure 6.**
*Dates of burning as obtained from the proposed dating algorithm (left panel) and as derived from dates of observation of hotspots by the SEVIRI instrument (right panel).*
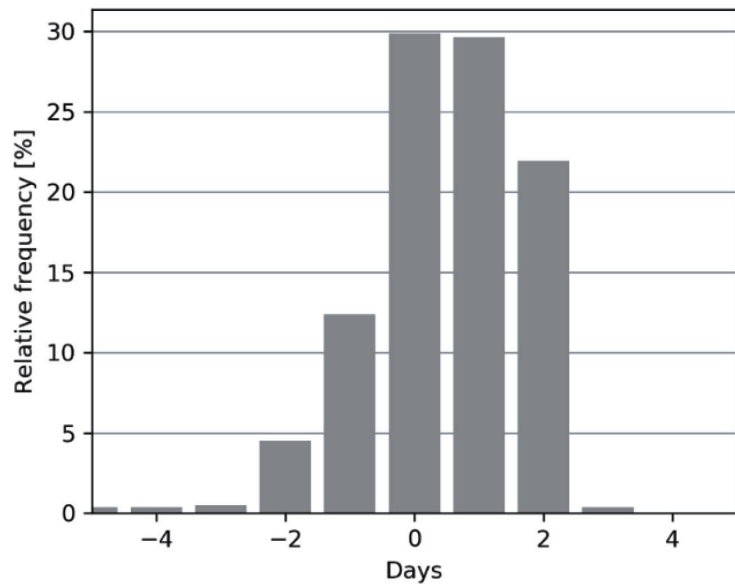


**Figure 7.**
*Histogram of difference between dates assigned by the proposed methodology and dates derived from hotspots identified by the SEVIRI instrument.*

2 months and a much wider area, covering a very large number of scars, and not a single one as in the present study. Regarding the estimated days of burning, 75% of estimated dates in the same study [64] presented deviations less than ±5 days from dates derived from hotspots identified by MODIS.

## 5. Conclusions

Using TOA values of MIR and TIR radiances and NIR reflectance from VIIRS 375m imagery, a set of optimal indices, V and W, were used to discriminate burned areas and to assign dates to every burned pixel. The ability of $v$ to discriminate between vegetated and non-vegetated surfaces may be used to build up composites of $w$ free from contamination by clouds, whereas the low values of W associated to burned surfaces suggest generating composites of minimum values of W to discriminate burned areas. Adopting this rationale, and in line with previous work [39, 64], discrimination of burned areas was performed using values ($W_{min}$) of a monthly composite of minimum of W and values ($\Delta W_{min}$) of

differences between that composite and the one of the previous month. First seed points are identified as the pixels that (1) are outliers in respect to pixel where no hotspots were identified, (2) present low values of $W_{min}$ characteristic of burning event, and (3) are associated to negative values of $\Delta W_{min}$, indicating a decrease of $W_{min}$ that is expected to occur after a burning event. New burned pixels are then successively aggregated using a seeded region-growing algorithm that starts with the previously identified seed points.

The algorithm was applied to the Monchique fire episode, a large event that occurred in southwestern Portugal during August 2018. The discriminative power of the algorithm was validated against the scar identified by Copernicus EMS303. Results obtained show that the (V, W) algorithm is suited to discriminate burned area over a mainland Portugal, supported by the good agreement, with a Dice coefficient of 0.933, between the burned area scar and the reference map. The commission and omission errors have values of 9 and 5%, respectively. Estimated dates of burning, obtained through analysis of time series of values of W, were compared against times of observation of hotspots obtained from the SEVIRI FRP product. About 70% of the estimated dates presented deviations of 1 day or less.

The development of reliable algorithms to discriminate and date burned areas is crucial for a better understanding of the biosphere-atmosphere interactions, for estimating burning emissions, for future projections of fire regime, and for mitigation and adaptation actions in Portugal, which is recurrently affected by severe fire events. In particular, accurate estimates of the date of burning are crucial when considering fire regime modeling, due to the constraint imposed by biomass availability into the spread of fire, and are also important for reducing uncertainties in biomass burning emissions [34]. The recent VIIRS sensor will allow the development of new burned area products at high spatial resolution, continuing and enhancing the imaging of the Earth initiated by the Advanced Very High-Resolution Radiometer (AVHRR) and the MODIS instruments. The present work represents a first attempt to assess the potential of using VIIRS imagery to identify burnt scars in Portugal. Results obtained in this work and in related previous ones pave the way to the generation of a long-term series of burned area maps containing accurate information about the extent, location, and time of occurrence of vegetation fires.

## Acknowledgements

## Conflict of interest

The authors declare they have no conflicts of interest.

## Author details

Carlos C. DaCamara[1]*, Renata Libonati[2,3], Miguel M. Pinto[1] and Alexandra Hurduc[1]

1 Faculdade de Ciências, Instituto Dom Luiz, Universidade de Lisboa, Lisboa, Portugal

2 Departmento de Meteorologia, Instituto de Geociências, Universidade Federal do Rio de Janeiro, Rio de Janeiro, Brazil

3 Centro de Estudos Florestais, Universidade de Lisboa, Lisboa, Portugal

*Address all correspondence to: cdcamara@fc.ul.pt

IntechOpen

## References

[1] Dentener F, Kinne S, Bond T, Boucher O, Cofala J, Generoso S, et al. Emissions of primary aerosol and precursor gases in the years 2000 and 1750 prescribed data-sets for AeroCom. Atmospheric Chemistry and Physics. 2006;**6**:4321-4344. DOI: 10.5194/acp-64321-2006

[2] Zhang J, Webster J, Powers RF, Mills J. Reforestation after the fountain fire in northern California: An untold success story. Journal of Forestry. 2008;**106**:425-430. DOI: 10.1093/jof/106.8.425

[3] van Leeuwen W, Casady G, Neary D, Bautista S, Alloza J, Carmel J, et al. Monitoring post-wildfire vegetation response with remotely sensed time series data in Spain, USA and Israel. International Journal of Wildland Fire. 2010;**19**:75-93. DOI: 10.1071/WF08078

[4] Bowman DMJS, Balch JK, Artaxo P, Bond WJ, Carlson JM, Cochrane MA, et al. Fire in the Earth system. Science. 2009;**324**(5926):481-484. DOI: 10.1126/science.1163886

[5] Storelvmo T, Leirvik T, Lohmann U, Phillips PC, Wild M. Disentangling greenhouse warming and aerosol cooling to reveal Earth's climate sensitivity. Nature Geoscience. 2016;**9**(4):286. DOI: 10.1038/ngeo2670

[6] Andreae MO, Rosenfeld D, Artaxo P, Costa AA, Frank GP, Longo KM, et al. Smoking rain clouds over the Amazon. Science. 2004;**303**:1337-1342. DOI: 10.1126/science.1092779. DOI: 10.1126/science.1092779

[7] Lohmann U, Rotstayn L, Storelvmo T, Jones A, Menon S, Quaas J, et al. Total aerosol effect: Radiative forcing or radiative flux perturbation? Atmospheric Chemistry and Physics. 2010;**10**(7):3235-3246. DOI: 10.5194/acp-10-3235-2010

[8] Certini G. Effects of fire on properties of forest soils: A review. Oecologia. 2005;**143**(1):1-10. DOI: 10.1007/s00442-004-1788-8

[9] Rosenfeld D. TRMM observed first direct evidence of smoke from forest fires inhibiting rainfall. Geophysical Research Letters. 1999;**26**(20):3105-3108. DOI: 10.1029/1999GL006066

[10] Menon S, Hansen J, Nazarenko L, Luo Y. Climate effects of black carbon aerosols in China and India. Science. 2002;**297**:2250-2253. DOI: 10.1126/science.1075159

[11] Koren I, Kaufman YJ, Remer LA, Martins JV. Measurement of the effect of Amazon smoke on inhibition of cloud formation. Science. 2004;**303**:1342-1345. DOI: 10.1126/science.1089424

[12] Fisher B, Turner RK, Morling P. Defining and classifying ecosystem services for decision making. Ecological Economics. 2009;**68**(3):643-653. DOI: 10.1016/j.ecolecon.2008.09.014

[13] Driscoll D, Lindenmayer D, Bennett AF, Bode M, Bradstoc RA, Cary G, et al. Fire management for biodiversity conservation: Key research questions and our capacity to answer them. Biological Conservation. 2010;**143**(9):1928-1939. DOI: 10.1016/j.biocon.2010.05.026

[14] Sellers PJ, Bounoua L, Collatz GJ, Randall DA, Dazlich DA, Los SO, et al. Comparison of radiative and physiological effects of doubled atmospheric $CO_2$ on climate. Science. 1996;**271**:1402-1406. DOI: 10.1126/science.271.5254.1402

[15] Jin Y, Roy DP. Fire-induced albedo change and its radiative forcing at the surface in northern Australia. Geophysical Research

Letters. 2005;**32**:L13401. DOI: 10.1029/2005GL022822

[16] Lambin EF, Geist HJ. Land-Use and Land-Cover Change. Local Processes and Global Impacts. Berlin: Springer Science & Business Media; 2008. p. WP6319

[17] Bowman DMJS, Johnston FH. Wildfire smoke, fire management, and human health. EcoHealth. 2005;**2**(1):76-80. DOI: 10.1007/s10393-004-0149-8

[18] Fowler CT. Human health impacts of forest fires in the southern United States: A literature review. Journal of Ecological Anthropology. 2003;**7**(1):39-63. DOI: 10.5038/2162-4593.7.1.3

[19] Patz JA, Engelberg D, Last J. The effects of changing weather on public health. Annual Review of Public Health. 2000;**21**(1):271-307. DOI: 10.1146/annurev.publhealth.21.1.271

[20] Bowman D. Wildfire science is at a loss for comprehensive data. Nature. 2018;**560**:7. DOI: 10.1038/d41586-018-05840-4

[21] Andela N, Morton DC, Giglio L, Chen Y, Van Der Werf GR, Kasibhatla PS, et al. A human-driven decline in global burned area. Science. 2017;**356**:1356-1362. DOI: 10.1126/science.aal4108

[22] Flannigan MD, Krawchuk MA, de Groot WJ, Wotton BM, Gowman LM. Implications of changing climate for global wildland fire. International Journal of Wildland Fire. 2009;**18**(5):483-507. DOI: 10.1071/WF08187

[23] Langmann B, Duncan B, Textor C, Trentmann J, van der Werf GR. Vegetation fire emissions and their impact on air pollution and climate. Atmospheric Environment. 2009;**43**(1):107-116. DOI: 10.1016/j.atmosenv.2008.09.047

[24] Kochi I, Donovan GH, Champ PA, Loomis JB. The economic cost of adverse health effects from wildfire-smoke exposure: A review. International Journal of Wildland Fire. 2010;**19**(7):803-817. DOI: 10.1071/WF09077

[25] Bowman DM, Balch J, Artaxo P, Bond WJ, Cochrane MA, D'Antonio CM, et al. The human dimension of fire regimes on Earth. Journal of Biogeography. 2011;**38**(12):2223-2236. DOI: 10.1111/j.1365-2699.2011.02595.x

[26] Johnston FH, Henderson SB, Chen Y, Randerson JT, Marlier M, DeFries RS, et al. Estimated global mortality attributable to smoke from landscape fires. Environmental Health Perspectives. 2012;**120**(5):695. DOI: 10.1289/ehp.1104422

[27] Pacheco AP, Claro J, Fernandes PM, de Neufville R, Oliveira TM, Borges JG, et al. Cohesive fire management within an uncertain environment: A review of risk handling and decision support systems. Forest Ecology and Management. 2015;**347**:1-17. DOI: 10.1016/j.foreco.2015.02.033

[28] Nogueira J, Ruffault J, Chuvieco E, Mouillot F. Can we go beyond burned area in the assessment of global remote sensing products with fire patch metrics? Remote Sensing. 2016;**9**(1):7. DOI: 10.3390/rs9010007

[29] Alonso-Canas I, Chuvieco E. Global burned area mapping from ENVISAT-MERIS and MODIS active fire data. Remote Sensing of Environment. 2015;**163**:140-152. DOI: 10.1016/j.rse.2015.03.011

[30] Giglio L, Boschetti L, Roy DP, Humber ML, Justice CO. The collection 6 MODIS burned area mapping algorithm and product. Remote Sensing of Environment. 2018;**217**:72-85. DOI: 10.1016/j.rse.2018.08.005

[31] Pereira AA, Pereira J, Libonati R, Oom D, Setzer AW, Morelli F, et al. Burned area mapping in the Brazilian savanna using a one-class support vector machine trained by active fires. Remote Sensing. 2017;**9**(11):1161. DOI: 10.3390/rs9111161

[32] Kasischke ES, French NHF, Harrell P, Christensen NL Jr, Ustin SL, Barry D. Monitoring of wildfires in boreal forests using large area AVHRR NDVI composite image data. Remote Sensing of Environment. 1993;**45**:61-71

[33] Pereira JMC. A comparative evaluation of NOAA/AVHRR vegetation indices for burned surface detection and mapping. IEEE Transactions on Geoscience and Remote Sensing. 1999;**37**(1):217-226. DOI: 10.1109/36.739156

[34] Mouillot F, Schultz MG, Yue C, Cadule P, Tansey K, Ciais P, et al. Ten years of global burned area products from spaceborne remote sensing—A review: Analysis of user needs and recommendations for future developments. International Journal of Applied Earth Observation and Geoinformation. 2014;**26**:64-79. DOI: 10.1016/j.jag.2013.05.014

[35] Tansey K, Gregoire JM, Defourny P, Leigh R, Pekel JFO, van Bogaert E, et al. A new, global, multi-annual (2000-2007) burnt area product at 1 km resolution. Geophysical Research Letters. 2018;**35**:1. DOI: 10.1029/2007GL031567

[36] Plummer S, Arino O, Simon M, Steffen W. Establishing an earth observation product service for the terrestrial carbon community: The GLOBCARBON initiative. Mitigation and Adaptation Strategies for Global Change. 2006;**11**:97-111. DOI: 10.1007/s11027-006-1012-8

[37] Roy DP, Boschetti L, Justice CO, Ju J. The collection 5 MODIS burned area product: Global evaluation by comparison with the MODIS active fire product. Remote Sensing of Environment. 2008;**112**:3690-3707. DOI: 10.1016/j.rse.2008.05.013

[38] Giglio L, Randerson JT, van der Werf GR, Kasibhatla PS, Collatz GJ, Morton DC, et al. Assessing variability and long-term trends in burned area by merging multiple satellite fire products. Biogeosciences. 2010;**7**:1171-1186. DOI: 10.5194/bg-7-1171-2010

[39] Libonati R, DaCamara CC, Setzer AW, Morelli F, Melchiori AE. An algorithm for burned area detection in the Brazil Cerrado using 4 μm MODIS imagery. Remote Sensing. 2015;**7**:15782-15803. DOI: 10.3390/rs71115782

[40] Chuvieco E, Lizundia-Loiola J, Pettinari ML, Ramo R, Padilla M, Mouillot F, et al. Generation and analysis of a new global burned area product based on MODIS 250 m reflectance bands and thermal anomalies. Earth System Science Data Discussions. 2018;**512**:1-24. DOI: 10.5194/essd-2018-46

[41] Trigg S, Flasse S. Characterising the spectral-temporal response of burned savannah using in situ spectroradiometry and infrared thermometry. International Journal of Remote Sensing. 2000;**21**:3161-3168. DOI: 10.1080/01431160050145045

[42] Verstraete MM, Pinty M. Designing optimal spectral indexes for remote sensing applications. IEEE Transactions on Geoscience and Remote Sensing. 1996;(5):1254-1265. DOI: 10.1109/36.536541

[43] Isabel MDPM. Cartografía e inventario de incendios forestales en la Península Ibérica a partir de imágenes NOAA-AVHRR. Universidad de Alcalá de Henares; 1999

[44] Martín MP, Gómez I, Chuvieco E. Performance of a burned-area index

(BAIM) for mapping Mediterranean burned scars from MODIS data. In: Proceedings of the 5th International Workshop on Remote Sensing and GIS Applications to Forest Fire Management: Fire Effects Assessment. Paris: Universidad de Zaragoza, GOFC GOLD, EARSeL; 2005. pp. 193-198

[45] Alleaume S, Hely C, Le Roux J, Korontzi S, Swap RJ, Shugart HH, et al. Using MODIS to evaluate heterogeneity of biomass burning in southern African savannahs: A case study. International Journal of Remote Sensing. 2005;**26**:4219-4237. DOI: 10.1080/01431160500113492

[46] USGS. Product Guide: Landsat surface reflectance-derived spectral indices [Internet]. 2007. Available from: https://landsat.usgs.gov/sites/default/files/documents/si_product_guide.pdf [Accessed: October 28, 2018]

[47] Loboda T, O'Neal KJ, Csiszar I. Regionally adaptable dNBR-based algorithm for burned area mapping from MODIS data. Remote Sensing of Environment. 2007;**109**:429-442. DOI: 10.1016/j.rse.2007.01.017

[48] Miller JD, Yool SR. Mapping forest post-fire canopy consumption in several overstory types using multi-temporal Landsat TM and ETM data. Remote Sensing of Environment. 2002;**82**(2-3):481-496. DOI: 10.1016/S0034-4257(02)00071-8

[49] Boer MM, Macfarlane C, Norris J, Sadler RJ, Wallace J, Grierson PF. Mapping burned areas and burn severity patterns in SW Australian eucalypt forest using remotely-sensed changes in leaf area index. Remote Sensing of Environment. 2008;**112**:4358-4396. DOI: 10.1015/j.rse.2008.08.005

[50] Miller JD, Thode AE. Quantifying burn severity in a heterogeneous landscape with a relative version of the delta normalized burn ratio (dNBR). Remote Sensing of Environment. 2007;**109**:66-80. DOI: 10.1016/j.rse.2006.12.006

[51] Bastarrika A, Chuvieco E, Martín MP. Mapping burned areas from Landsat TM/ETM+ data with a two phase algorithm: Balancing omission and commission errors. Remote Sensing of Environment. 2011;**105**:1003-1012. DOI: 10.1016/j.rse.2010.12.005

[52] Trigg S, Flasse S. An evaluation of different bi-spectral spaces for discriminating burned shrub-savannah. International Journal of Remote Sensing. 2001;**22**(13):2641-2647. DOI: 10.1080/01431160110053185

[53] Libonati R, DaCamara CC, Pereira JMC, Peres LF. On a new coordinate system for improved discrimination of vegetation and burned areas using MIR/NIR information. Remote Sensing of Environment. 2011;**114**:831-843. DOI: 10.1016/j.rse.2011.02.006

[54] DaCamara CC, Libonati R, Ermida SL, Calado TJ. A user-oriented simplification of the (V, W) burn-sensitive vegetation index system. IEEE Geoscience and Remote Sensing Letters. 2016;**13**(12):1822-1826. DOI: 10.1109/LGRS.2016.2614319

[55] NASA. Data Product User Guide for Suomi-National Polar-Orbiting Partnership (S-NPP) Sounder Science Investigator-led Processing System (SIPS) Advanced Technology Microwave Sounder (ATMS) Level 1B Products [Internet]. 2017. Available from: https://docserver.gesdisc.eosdis.nasa.gov/repository/Mission/SNPP_Sounder/3.3_ScienceDataProductDocumentation/3.3.4_ProductGenerationAlgorithms/ATMS_Readme_Vers_1_20170508.pdf [Accessed: October 28, 2018]

[56] NASA. Visible Infrared Imaging Radiometer Suite (VIIRS) 375 m &

750 m Active Fire Detection Data Sets Based on NASA VIIRS Land Science Investigator Processing System (SIPS) Reprocessed Data—Version 1 [Internet]. 2017. Available from: https://lpdaac.usgs.gov/sites/default/files/public/product_documentation/vnp14_user_guide_v1.3.pdf [Accessed: October 28, 2018]

[57] Kaufman YJ, Remer LA. Detection of forests using MID-IR reflectance: An application for aerosol studies. IEEE Transactions on Geoscience and Remote Sensing. 1994;**32**:672-683. DOI: 10.1109/36.297984

[58] Schroeder W, Oliva P, Giglio L, Csiszar IA. The new VIIRS 375 m active fire detection data product: Algorithm description and initial assessment. Remote Sensing of Environment. 2014;**143**:85-96. DOI: 10.1016/j.rse.2013.12.008

[59] Wooster MJ, Roberts G, Freeborn PH, Xu W, Govaerts Y, Beeby R, et al. LSA SAF Meteosat FRP products—Part 1: Algorithms, product contents, and analysis. Atmospheric Chemistry and Physics. 2015;**15**(22):13217-13239. DOI: 10.5194/acp-15-13217-2015

[60] Copernicus. Emergency Management Service [Internet]. 2018. Available from: http://emergency.copernicus.eu/ [Accessed: October 28, 2018]

[61] Hantson S, Padilla M, Cort D, Chuvieco E. Strengths and weaknesses of MODIS hotspots to characterize global fire occurrence. Remote Sensing of Environment. 2013;**131**:152-159. DOI: 10.1016/j.rse.2012.12.004

[62] Mahalanobis PC. On the generalised distance in statistics. Proceedings of the National Institute of Sciences of India. 1936;**2**(1):49-55

[63] Wilks DS. Statistical Methods in the Atmospheric Sciences. Vol. 100. Oxford: Academic Press; 2006. 676 pp

[64] Panisset J, DaCamara CC, Libonati R, Peres LF, Calado TJ, Barros A. Assigning dates and identifying areas affected by fires in Portugal based on MODIS data. Anais da Academia Brasileira de Ciências. 2017;**89**(3):1487-1501. DOI: 10.1590/0001-3765201720160707

[65] Giglio L, Loboda T, Roy DP, Quayle B, Justice CO. An active-fire based burned area mapping algorithm for the MODIS sensor. Remote Sensing of Environment. 2009;**113**:408-420. DOI: 10.1016/j.rse.2008.10.006

[66] Roberts G, Wooster MJ, Xu W, Freeborn PH, Morcrette JJ, Jones L, et al. LSA SAF Meteosat FRP products—Part 2: Evaluation and demonstration for use in the Copernicus Atmosphere Monitoring Service (CAMS). Atmospheric Chemistry and Physics. 2015;**15**:13241-13267. DOI: 10.5194/acp-15-13241-2015